ARTICLE Open Access

Implementation of threshold- and memory-switching memristors based on electrochemical metallization in an identical ferroelectric electrolyte

Chansoo Yoon[1], Gwangtaek Oh[1], Sohwi Kim[1], Jihoon Jeon[1], Ji Hye Lee[2,3], Young Heon Kim[4] and Bae Ho Park[1]

Abstract

The use of an identical electrolyte in electrochemical metallization (ECM)-based neuron and synaptic devices has not yet been achieved due to their different resistive-switching characteristics. Herein, we describe ECM devices comprising the same ferroelectric $PbZr_{0.52}Ti_{0.48}O_3$ (PZT) electrolyte, which can sustain both neuron and synaptic behavior depending on the identity of the active electrode. The Ag/PZT/$La_{0.8}Sr_{0.2}MnO_3$ (LSMO) threshold switching memristor shows abrupt and volatile resistive switching characteristics, which lead to neuron devices with stochastic integration-and-fire behavior, auto-recovery, and rapid operation. In contrast, the Ni/PZT/LSMO memory switching memristor exhibits gradual, non-volatile resistive switching behavior, which leads to synaptic devices with a high on/off ratio, low on-state current, low variability, and spike-timing-dependent plasticity (STDP). The divergent behavior of the ECM devices is attributed to greater control of cation migration through the ultrathin ferroelectric PZT. Thus, ECM devices with an identical ferroelectric electrolyte offer promise as essential building blocks in the construction of high-performance neuromorphic computing systems.

Introduction

Hardware implementation of artificial neural networks (ANNs) requires the development of neuron and synaptic devices. Neuronal devices must deliver abrupt and volatile current updates, integration-and-firing with stochastic behavior, auto-recovery, and rapid operation[1–3]. Threshold switching based on electrochemical metallization (ECM)[2–4], Mott-transition[5–7], and phase-change behavior[1]-based memristors has been used to implement neuron devices with reliable performance. Synaptic devices should afford non-volatile, analog current updates with a high on/off ratio, minimal device variability, low readout current, and synaptic plasticity, including spike-timing-dependent plasticity (STDP)[8–12]. Non-volatile memory switching based on ECM[10,13–15], valence-change memory[16,17], electrolyte-based transistors[18–20], and ferroelectric polarization reversal[21,22] have been employed to implement synaptic devices. Although several types of architectures have been used to assemble ANNs, neuron and synaptic devices have typically been developed separately using a wide variety of materials and processes[1–3,10,18,21,22], leading to limited scalability, complex structures and processes, and excessive cost.

The foregoing problems can be solved by introducing a memristor with threshold- and memory-switching controlled by manageable components. If neuron and synaptic devices can be implemented concurrently using ECM-based memristors with identical electrolyte layers, then they can become simplified fundamental building blocks in the design and fabrication of large-scale ANNs for future reconfigurable neuromorphic systems[23]. A prominent challenge in the development of such devices is poorly controlled cation migration through the electrolyte layer, which leads to random formation (set) of the

Correspondence: Bae Ho Park (baehpark@konkuk.ac.kr)
[1]Division of Quantum Phases & Devices, Department of Physics, Konkuk University, Seoul 143-701, Republic of Korea
[2]Center for Correlated Electron Systems (CCES), Institute of Basic Science (IBS), Seoul 08826, Republic of Korea
Full list of author information is available at the end of the article

© The Author(s) 2023

Open Access This article is licensed under a Creative Commons Attribution 4.0 International License, which permits use, sharing, adaptation, distribution and reproduction in any medium or format, as long as you give appropriate credit to the original author(s) and the source, provide a link to the Creative Commons license, and indicate if changes were made. The images or other third party material in this article are included in the article's Creative Commons license, unless indicated otherwise in a credit line to the material. If material is not included in the article's Creative Commons license and your intended use is not permitted by statutory regulation or exceeds the permitted use, you will need to obtain permission directly from the copyright holder. To view a copy of this license, visit http://creativecommons.org/licenses/by/4.0/.

conduction channel[10]. Therefore, cation migration must be harnessed to establish controllable set processes in ECM memristors and achieve simultaneous neuronal and synaptic operation.

Herein, we demonstrate the concurrent implementation of threshold and memory switching memristors based on ECM with identical electrolyte layers, which are Ag, Cu, and Ni/$PbZr_{0.52}Ti_{0.48}O_3$ (PZT)/$La_{0.8}Sr_{0.2}MnO_3$ (LSMO) with an ultrathin ferroelectric PZT. Because LSMO is located near the phase boundary, it exhibits desirable semiconducting behavior and high conductivity for a high-performance memristor. We introduce polarization-bound charges of the ferroelectric layer for greater control of cation migration and set process in an ECM memristor. The Ag/PZT/LSMO memristor shows abrupt and volatile resistive switching (RS) due to rapid cation migration and can provide integration and firing with stochastic behavior and auto-recovery at a 100ns rate. In contrast, the Ni/PZT/LSMO memristor exhibits gradual and non-volatile RS due to the low velocity of cation migration, which emulates synaptic plasticity with very low variability (i.e., temporal variations of <1.0 and <2.0% for potentiation and depression, respectively, during $>2.7 \times 10^4$ identical write-read pulse cycles in 105 devices). In addition, Ni/PZT/LSMO displays a large analog on/off ratio of $\sim10^2$, a low on-state current of ~10 nA, long-term memory for >80000 s, and STDP. Thus, our identical electrolyte-based system represents major progress toward the development of large-scale ANNs with high scalability, simple structure, and low cost.

Materials and methods

Growth of PZT/LSMO

PZT/LSMO heterostructures were grown on single-crystalline $SrTiO_3$ (STO) (001) substrates using pulsed laser deposition with a KrF excimer laser (248 nm wavelength). The laser beam was irradiated on the rotating LSMO and PZT targets at an energy density of ~0.625 J/cm^2 with a 1 Hz repetition rate. LSMO and PZT thin films were deposited at 675 and 550 °C under oxygen pressures of 100 and 200 mTorr, respectively. Such a low laser energy density was used to increase the concentration of defects in the PZT layer based on the comparatively high vapor pressure of PbO[24]. The PZT/LSMO heterostructure was annealed for 90 min at 550 °C under an oxygen pressure of 500 mTorr and cooled at 5 °C/min. Top electrode (TE) fabrication was accomplished by establishing a 30 nm-thick Ag, Cu, Ni, or Pt layer on the PZT/LSMO heterostructure using e-beam lithography, e-beam evaporation (Ag, Cu, Ni) or sputtering (Pt), and a lift-off process. For active-metal TEs, a 25 nm Au film was deposited in situ as a capping layer directly on Ag, Cu, or Ni.

Structural characteristics

HR-TEM cross-section images were obtained using a 300-kV field-emission TEM (Tecnai G^2 F30 Supertwin). Film thicknesses were determined using HR-TEM images.

Piezoresponse force microscopy

PFM images and local hysteresis loops were obtained using a commercial AFM (Park Systems, XE-100) with a Pt/Ir-coated cantilever. A lock-in amplifier (Stanford Research Systems, SR 830) was used to apply the ac probe voltage ($f = 17$ kHz) with a 1.0-V (peak-to-peak) amplitude in the PFM mode.

Electrical measurements

I-V characteristics were measured using an AFM (Seiko, SPA-300HV) equipped with a semiconductor parameter analyzer (Agilent, 4156B) in the dc voltage sweep mode. A pulse stimulus was applied in pulse mode with gradual current modulation using an AFM equipped with a semiconductor characterization system (Keithley, 4200-SCS). All electrical measurements at room temperature were performed in air using a diamond-coated cantilever. Temperature-dependent *I-V* characteristics were measured using an AFM (Seiko, SPA-300HV) equipped with a semiconductor parameter analyzer (Agilent, 4156B) in dc voltage sweep mode under vacuum ($\sim3.0 \times 10^{-2}$ mbar) to avoid side effects such as oxidation. The relationship between positive metal-ion migration and the direction of ferroelectric polarization in the PZT was explored by comparing the change in current at opposite polarization directions. External voltages of 5.0 and −5.0 V were applied to the active-metal electrode to achieve downward and upward polarizations, respectively. For downward polarization, 50 successive negative pulses were applied at −0.4 V amplitude and 0.15-s duration to obtain HRS without polarization reversal in the Ag, Cu, and Ni/PZT/LSMO structures. Thereafter, consecutive 0.5-V amplitude and 0.7-s duration stimulation pulses were applied to induce potentiation.

Conductive-AFM (CAFM)

Active-metal-coated cantilevers were established on the diamond-coated cantilever using e-beam evaporation (Ag, Cu, or Ni) to investigate the configuration of the conduction channel. After measuring each *I-V* hysteresis loop, CAFM mapping images were obtained using an AFM (Seiko, SPA-300HV) with a −1.0 V dc reading voltage applied to the bottom electrode during 1 Hz scanning in vacuum ($\sim3.0 \times 10^{-2}$ mbar).

Temporal variation of analog switching

Temporal variation represents the degree of variation during conductance potentiation or depression. The temporal variation in analog switching was estimated by

use of the following equations[25]:

$$\text{potentiation}: G_{(n+1)} = G_{(n)} + \triangle G_{p} \quad (1)$$

$$\triangle G_{P} = \left(B\left(1 - e^{\left(-\frac{P_{(n+1)}}{A}\right)}\right) - B\left(1 - e^{\left(-\frac{P_{(n)}}{A}\right)}\right)\right) + \sigma_{P} \quad (2)$$

$$\text{depression}: G_{(n+1)} = G_{(n)} + \triangle G_{d} \quad (3)$$

$$\triangle G_{d} = \left(B\left(1 - e^{\left(-\frac{P_{(n+1)}}{A}\right)}\right) - B\left(1 - e^{\left(-\frac{P_{(n)}}{A}\right)}\right)\right) + \sigma_{D} \quad (4)$$

$$B = \frac{G_{max} - G_{min}}{1 - e^{\frac{-P_{max}}{A}}} \quad (5)$$

where $G_{(n+1)}$ and $G_{(n)}$ represent the conductance values of the device when pulse stimulations, and $P_{(n+1)}$ and $P_{(n)}$, respectively, are applied. G_{max}, G_{min}, and P_{max}, which are extracted directly from the experimental data, represent the maximum conductance, minimum conductance, and maximum pulse number required to switch the device between the minimum and maximum conductance states, respectively. A is a parameter that controls the nonlinear characteristic of the weight update, and B is a function of A for fitting the functions within the ranges of G_{max}, G_{min}, and P_{max}. σ_P and σ_D are parameters related to the temporal variation of potentiation and depression, respectively. σ is the product of the temporal variation and Randn, which is a normalized random number. Figure 4d shows the fits of the potentiation and depression curves using the above formulas for temporal variations of 0.1, 1.0, 2.0, 3.0, 4.0, and 5.0%.

Results and discussion

Mechanism of the ECM memristor

The operating mechanism of conventional ECM memristors is based on the formation and rupture of nanoscale conduction channels comprising the metallic elements (Ag, Cu, or Ni) of an active top electrode (TE)[26–30]. Figure 1a shows that when a positive bias is applied to the TE, the metal is oxidized to the metal ion. The metal ions of charge, q, move under the influence of the net potential of the constituent ions and are assumed to have the hopping distance (a) and activation energy (E_a) shown in the energy diagram. The application of an electric field (E) modifies the potential well and results in a change in the effective barrier by $\pm \frac{1}{2}qaE$, which is aligned with (−) and opposed to (+) the direction of the electric field. Therefore, the applied field exponentially accelerates cation migration, as described by Eq. (1)[29,31,32],

$$v = a \cdot f \cdot \exp(-E_a/kT) \cdot \sinh(qaE/2kT) \quad (6)$$

where v is the drift velocity of the cation, f is the attempt frequency, k is the Boltzmann constant, and T is the absolute temperature. In this process, a and E_a properties of the cation, as well as E, can influence the drift velocity via changes in the growth rate, density, and width of the conduction channel[33–35]. Reduction of the ejected metal ions to their elemental state leads to the nucleation and growth of a nanoscale conduction channel. The conduction channel grows until it reaches a maximum length and width, which defines the set process[31,36]. Under a negative bias, rupture of the conduction channel occurs due to a thermally assisted electrochemical reaction, which is the reset process[14,34,35]. The introduction of ferroelectric PZT as an electrolyte material for positive metal-ion migration induces an additional electric field via ferroelectric polarization of the bound charges and provides greater control of metal-ion migration[14]. In addition, conductive channels comprising different metals exhibit different growth modes and structures with the same electrolyte material[13,35,37]. Thus, we expect that the length and width of conduction channels can be effectively regulated by changing the active electrode material and by introducing a ferroelectric electrolyte.

RS behaviors of different metal/PZT/LSMO structures

We have confirmed the stable ferroelectricity of PZT using piezoresponse force microscopy (PFM). The top panels of Fig. 1b show the out-of-plane PFM phase and amplitude images of the PZT film. The PFM phase image reveals bright and dark regions corresponding to the outer and inner squares, respectively, which indicates that the two areas exhibit opposing directions of ferroelectric polarization. The domain structure does not change significantly after 3 h, which demonstrates its room-temperature stability (bottom panels, Fig. 1b). We observed similar ferroelectric domain structures on PZT films with different thicknesses (Supplementary Fig. S1). We also investigated the local out-of-plane ferroelectric characteristics of the PZT film (Supplementary Fig. S2). The epitaxial growth of the PZT (5.0 nm) and LSMO (8.0 nm) films is confirmed by the well-aligned lattices in the high-resolution transmission electron microscopy image (Fig. 1c). Ultrathin PZT is used for low operation voltage, resulting in reduced energy consumption. Moreover, to ensure high scalability, we included a thin bottom electrode.

We obtained current-voltage (I-V) curves to characterize the RS behavior of the Ag, Cu, or Ni/PZT/LSMO structures. The Ag/PZT/LSMO device exhibits a threshold switching behavior, where both abrupt set-

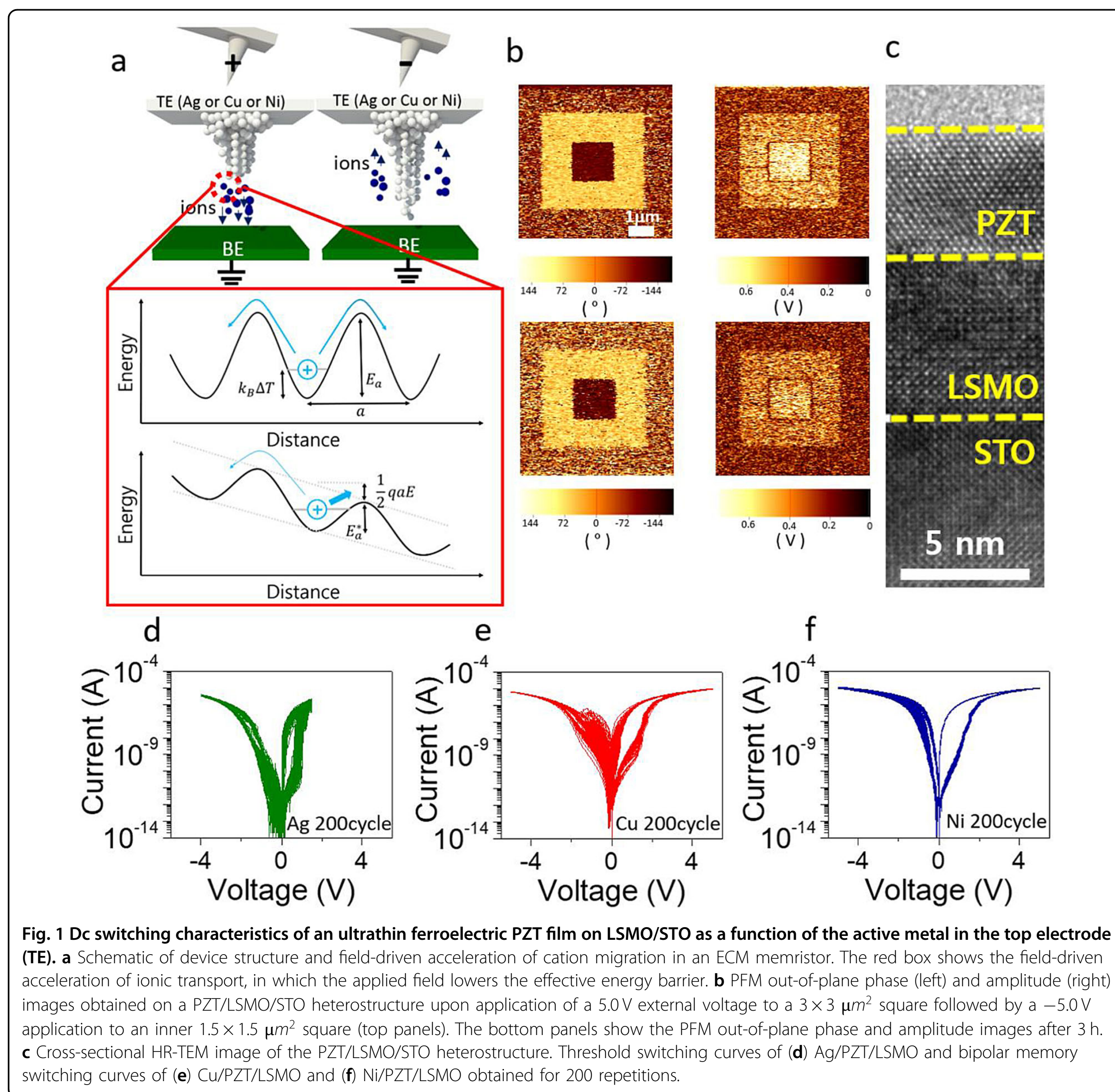

Fig. 1 Dc switching characteristics of an ultrathin ferroelectric PZT film on LSMO/STO as a function of the active metal in the top electrode (TE). a Schematic of device structure and field-driven acceleration of cation migration in an ECM memristor. The red box shows the field-driven acceleration of ionic transport, in which the applied field lowers the effective energy barrier. **b** PFM out-of-plane phase (left) and amplitude (right) images obtained on a PZT/LSMO/STO heterostructure upon application of a 5.0 V external voltage to a 3×3 μm^2 square followed by a −5.0 V application to an inner 1.5×1.5 μm^2 square (top panels). The bottom panels show the PFM out-of-plane phase and amplitude images after 3 h. **c** Cross-sectional HR-TEM image of the PZT/LSMO/STO heterostructure. Threshold switching curves of (**d**) Ag/PZT/LSMO and bipolar memory switching curves of (**e**) Cu/PZT/LSMO and (**f**) Ni/PZT/LSMO obtained for 200 repetitions.

switching from a high-resistance (HRS) to low-resistance state (LRS) and auto-reset switching from the LRS to HRS occur at positive voltages (Fig. 1d) without a forming process. This behavior is also observed under consecutive positive DC sweep voltages without a negative DC sweep (Supplementary Fig. S3). By considering our previous report, which showed non-volatile RS in a Ag/PZT/LSMO device[14], the PZT in the current study was deposited using a lower laser fluence of ~ 0.625 J/cm^2 to induce lower E_a and higher drift velocity of the cation. On the other hand, the Cu/PZT/LSMO (Fig. 1e) and Ni/PZT/LSMO (Fig. 1f) devices show bipolar RS behavior, wherein gradual set and reset switching occur at positive and negative voltages, respectively, without a forming process. We observe similar trends in the RS behavior of devices with different PZT thicknesses (Supplementary Fig. S4).

For comparison, we fabricated a Pt/PZT/LSMO device with an inert Pt electrode, which is difficult to electrochemically dissolve[14,32]. This design exhibits switching in the direction opposite that of the Ag, Cu, or Ni/PZT/LSMO devices (Supplementary Fig. S5). Moreover, the LRS current value of the Ag, Cu, or Ni/PZT/LSMO assemblies does not depend on electrode size, whereas the HRS value decreases as electrode size decreases (Supplementary Fig. S6). This behavior suggests that the RS is

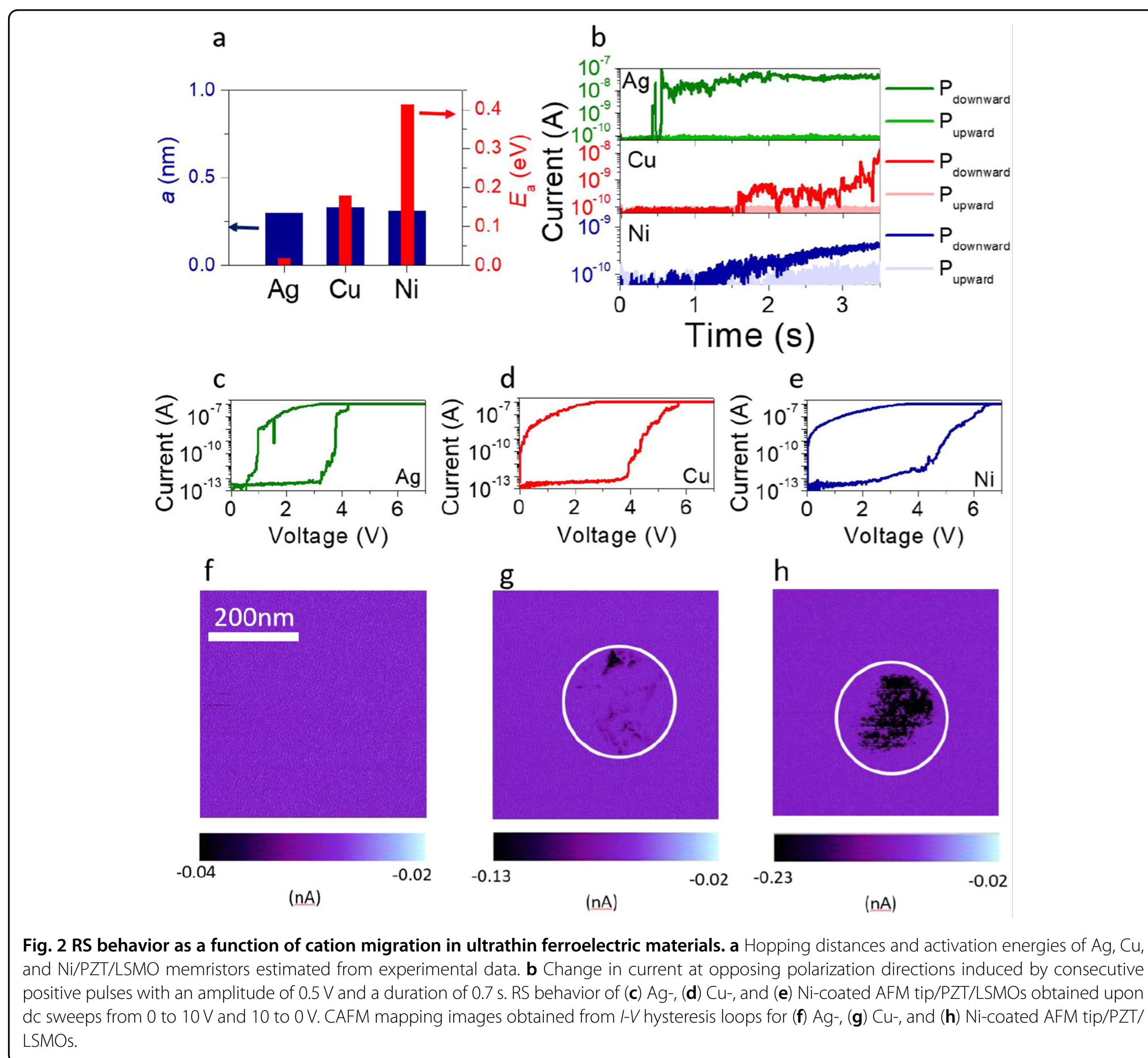

Fig. 2 RS behavior as a function of cation migration in ultrathin ferroelectric materials. a Hopping distances and activation energies of Ag, Cu, and Ni/PZT/LSMO memristors estimated from experimental data. **b** Change in current at opposing polarization directions induced by consecutive positive pulses with an amplitude of 0.5 V and a duration of 0.7 s. RS behavior of (**c**) Ag-, (**d**) Cu-, and (**e**) Ni-coated AFM tip/PZT/LSMOs obtained upon dc sweeps from 0 to 10 V and 10 to 0 V. CAFM mapping images obtained from *I-V* hysteresis loops for (**f**) Ag-, (**g**) Cu-, and (**h**) Ni-coated AFM tip/PZT/LSMOs.

caused by the formation and rupture of a conduction channel, as occurs in a conventional ECM device[14].

We performed experiments to estimate the parameters a and E_a, which significantly affect the drift velocity of metal ions. The a values of the Ag, Cu, and Ni/PZT/LSMO devices are 0.30, 0.33, and 0.31 nm, respectively (Fig. 2a). Because a/w is less than 0.2 in all devices, where w is the thickness of the PZT layer, ion hopping must be rate limiting (Supplementary Fig. S7)[38]. The E_a values for Ag, Cu, and Ni/PZT/LSMO are estimated to be 0.02, 0.18, and 0.41 eV, respectively (Supplementary Fig. S8). A possible explanation for the dependence of E_a on the metal in the TE is that a metal ion with higher charge will produce a greater Coulomb interaction and a larger activation energy[39,40]. Because the drift velocity is a function of the activation energy, it is expected that Ag ions with small activation energies present high drift velocities, while Ni ions with large activation energies present low drift velocities.

Abrupt set processes have been widely reported in conventional ECM memristors with different metal ions and non-ferroelectric electrolytes[41–44]. We presume that the gradual set switching behavior observed in Cu and Ni/PZT/LSMO is induced by the correlation between polarization bound charges and metal ions. Figure 2b shows that current levels increase upon consecutive pulsing at downward polarization in the PZT. The negative bound charges accumulate at the Ag, Cu or Ni/PZT interface and attract cations originating from the oxidation of active electrodes by an external positive bias. Then,

the cations can be reduced by free electrons passing through the PZT layer, leading to the growth of the conduction channel. In contrast, consecutive pulsing does not increase the HRS current at upward polarization, as found in a previous report (see Methods)[14]. The positive bound charges accumulated at the Ag, Cu or Ni/PZT interface repel cations from the active electrode, which hinders the growth of the conduction channel. The foregoing results suggest that the vertical growth of the conduction channel is strongly influenced by polarization bound charges at the interfaces.

We investigated the temperature-dependent RS behavior of Ag, Cu, and Ni/PZT/LSMOs (Supplementary Fig. S9). The LRS currents of all devices increase with temperature, contrary to the behavior of conventional ECM memristors[10,14,45]. This result indicates that migrating metal ions in our devices do not form complete conduction channels. Because Ag, Cu, and Ni/LSMO contacts without PZT show ohmic behavior (Supplementary Fig. S10), complete conduction channels formed in the Ag, Cu, and Ni/PZT/LSMO devices in the LRS should show ohmic *I-V* responses with decreasing current at increasing temperature. Vertical growth of the conduction channel is slow near the PZT/LSMO interface because positive metal ions are repelled by the positive bound charges arising from downward polarization. The gradual increase in current in the Ni/PZT/LSMO may result from a large E_a and downward polarization in the PZT leading to low drift velocity. If Ag ions with small E_a are present, an abrupt set process may be induced by their high drift velocity despite the repulsive force from positive bound charges at the PZT/LSMO interface.

The drift velocity of metal ions impacts the configuration of the conduction channel[33]. We performed conductive AFM (CAFM) measurements on PZT/LSMO structures using Ag-, Cu-, and Ni-coated AFM tips to establish the metal-ion dependence of the conduction channel configuration. The details of the electrical measurements and tip fabrication are provided in the Methods section. The Ag-coated tip/PZT/LSMO shows abrupt and volatile RS behavior, whereas the Cu- and Ni-coated tip/PZT/LSMOs exhibit gradual, nonvolatile RS behavior (Fig. 2c–e). For comparison, we also fabricated a diamond-coated tip/PZT/LSMO, which exhibited RS behavior in the opposite direction to those of the Ag, Cu, or Ni/PZT/LSMO structures (Supplementary Fig. S11). A CAFM mapping image was obtained after each *I-V* hysteresis loop. The CAFM image does not reveal a conduction channel for the Ag-coated tip/PZT/LSMO (Fig. 2f), which indicates rapid dissolution of a narrow, weak conduction channel induced by the high drift velocity of Ag ions. In contrast, clearly discernible conduction channels are observed in the CAFM images of Cu- and Ni-coated tip/PZT/LSMO structures, indicating the formation of wide, robust conduction channels induced by the low drift velocities of Cu and Ni ions. The wider conduction channel of the Ni-coated tip/PZT/LSMO relative to the Cu-coated tip/PZT/LSMO is attributed to the lower drift velocity of Ni ions relative to Cu ions. The high drift velocity of cations causes device variability[13,46]. The set-voltage and current-level distributions upon DC bias switching show low device variability for Ni/PZT/LSMO (Supplementary Fig. S12). Additionally, we also measured the analog switching of Cu/PZT/LSMO to investigate the effect of a drift velocity higher than that of Ni (Supplementary Fig. S13). The higher drift velocity of the Cu cation in the PZT electrolyte led to more stochastic characteristics, such as a more abrupt change in current.

Neuron device consisting of an Ag/PZT/LSMO memristor

Biological neurons conduct important signal-processing tasks by integrate-and-fire and auto-recovery[2,3]. These characteristics can be emulated by electronic devices, such as a conduction channel-based volatile RS device, for neuromorphic computing[2,3]. We measured the current responses following various stimulations applied to an Ag/PZT/LSMO memristor characterized by volatile RS behavior. When a sequence of 1.2-V sub-threshold pulses is applied to the device, firing occurs after a certain number of pulses (Supplementary Fig. S14). A DC sweep also induces a current response depending on the ramp rate of the sweep. Figure 3a–c display volatile RS behaviors with auto-recovery similar to those of a NbO_x-based neuron device[5]. The experimentally measured histograms of the response statistics in Fig. 3d–f show that the threshold is not sharp but has a probability distribution function similar to the stochastic behavior commonly observed in actual neurons[2]. An increase in the ramp rate produces a larger response-step number, faster auto-recovery, and a greater probability of no response. Similar behavior is observed in Ag/PZT/LSMO memristors with thicker PZT layers (Supplementary Figs. S15 and S16). To emulate the strength-dependent spiking probability of biological neurons[3], we measured the current spiking response using DC sweeps of different amplitudes. Figure 3g and 3i show that the spiking probability increases with increasing dc amplitude, which results from the various integration rates of Ag/PZT/LSMO at different dc amplitudes. Thus, our Ag/PZT/LSMO memristor mimics the stimulus-strength-dependent spiking probability of a biological neuron.

We also expect that enabling integrate-and-fire characteristics with ultrafast pulses may be achieved by the rapid drift velocity of Ag ions under a high electric field. Figures 3j and 3k display the current spiking responses. Although consecutive pulses with a 4.0-V amplitude do

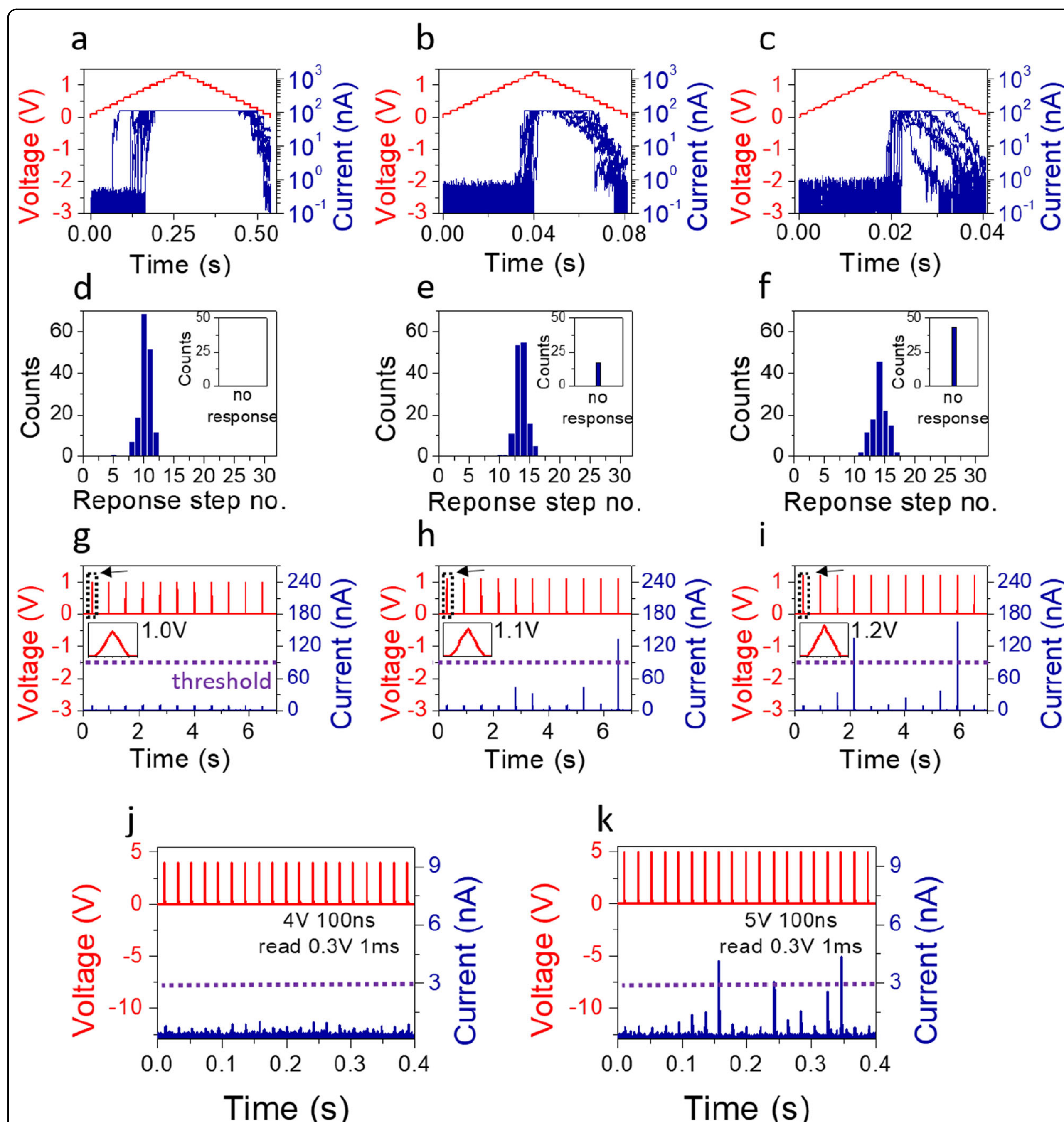

Fig. 3 Current response of an Ag/PZT/LSMO memristor upon consecutive electrical stimulations as a biological neuron mimic. a–f, (**a**–**c**) Current responses and (**d**–**f**) corresponding statistics upon DC sweeps at ramp rates of (**a, d**) 0.005 V/ms, (**b, e**) 0.034 V/ms, and (**c, f**) 0.068 V/ms. The insets of (**d**–**f**) show the no-response statistics. Spiking response of current upon repetitive DC sweeps at amplitudes of (**g**) 1.0, (**h**) 1.1, and (**i**) 1.2 V with a fixed dc sweep number (11) and ramp rate (0.1 V/ms). Spiking current responses upon consecutive pulses at amplitudes of (**j**) 4.0 and (**k**) 5.0 V with fixed pulse stimulation number (19), duration (100 ns), and interval (20 ms). A 1 ms, 0.3 V reading pulse was applied immediately after each programming pulse to measure the current response.

not induce a current spike, those with a 5.0-V amplitude induce current spiking and auto-recovery behavior, which replicates the integrate-and-fire and auto-recovery behavior at an ultrafast, 100 ns pulse duration. A high-speed artificial neuron is particularly useful in emerging applications such as the processing of event-based sensory information and energy-efficient large-scale neural networks[1,47].

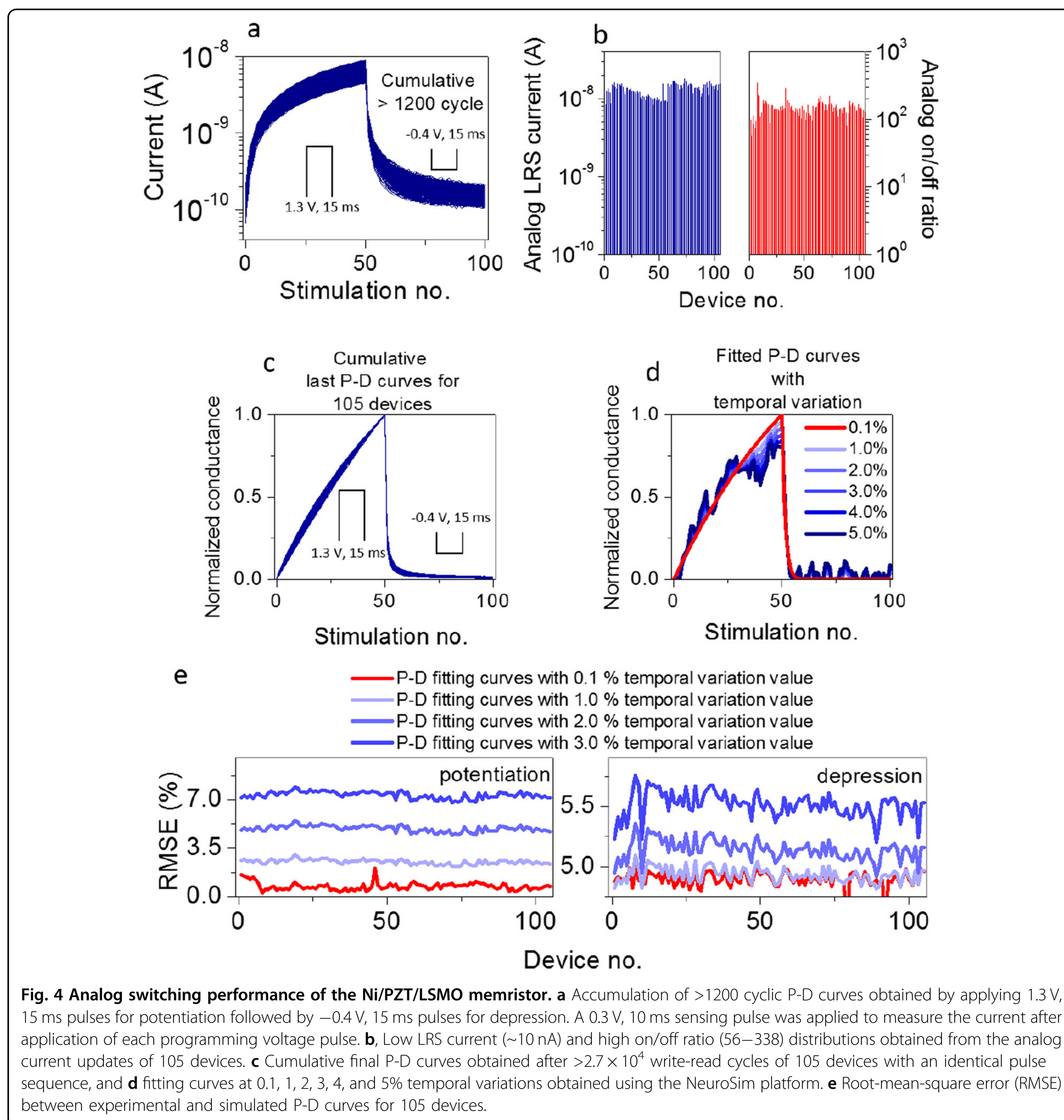

Fig. 4 Analog switching performance of the Ni/PZT/LSMO memristor. a Accumulation of >1200 cyclic P-D curves obtained by applying 1.3 V, 15 ms pulses for potentiation followed by −0.4 V, 15 ms pulses for depression. A 0.3 V, 10 ms sensing pulse was applied to measure the current after application of each programming voltage pulse. **b**, Low LRS current (~10 nA) and high on/off ratio (56−338) distributions obtained from the analog current updates of 105 devices. **c** Cumulative final P-D curves obtained after $>2.7 \times 10^4$ write-read cycles of 105 devices with an identical pulse sequence, and **d** fitting curves at 0.1, 1, 2, 3, 4, and 5% temporal variations obtained using the NeuroSim platform. **e** Root-mean-square error (RMSE) between experimental and simulated P-D curves for 105 devices.

Synaptic device comprising a Ni/PZT/LSMO memristor

The implementation of synaptic devices requires multilevel or gradually modulated resistance states[8–10]. We measured the updated current following voltage pulses applied to the Ni/PZT/LSMO memristor, which exhibited the most gradual change in current of the investigated memristor topologies. Figure 4a shows the accumulation of more than 1200 cyclic potentiation-depression (P-D) curves. The observed behavior supports the generation of a stable analog current upon application of a consistent pulse sequence. A high on/off ratio of 62 and a low LRS current level of 9×10^{-9} A are produced. We surmise that an incomplete conduction channel and a semiconducting LSMO bottom electrode induce the low read-out current of the analog LRS. Reproducible P-D curves can be obtained under various conditions and maintained even after $\sim 5.5 \times 10^5$ write-read operations (Supplementary Fig. S17). We also observed 270−300 stable cumulative P-D curves for all 105 devices (Supplementary Fig. S18). This result is consistent with the high on/off ratio (56−338) and low LRS

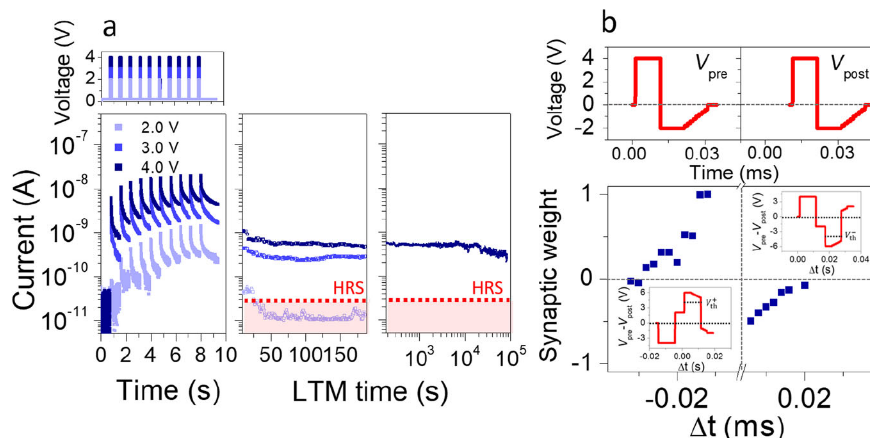

Fig. 5 Long-term memory and STDP of the Ni/PZT/LSMO memristor. a Time evolution of current obtained following 10 consecutive voltage pulses (duration=0.1 s, repetition rate=0.7 s) at 2.0-, 3.0-, and 4.0 V amplitudes. A total of 742 consecutive reading pulses (0.2 V amplitude, 1 ms duration) were applied after each programming pulse to measure the current evolution. **b** Experimental STDP curves (bottom panel) induced by pre- and postneuron spikes with the voltage waveforms shown in the top panels as a function of the delay time, $\triangle$t. The inset shows the superposed $V_{pre} - V_{post}$ when Δt is negative (left inset) and positive (right inset). If the $V_{pre} - V_{post}$ value exceeds the corresponding threshold voltage (V_{th}^+ or V_{th}^-), the synaptic weight will increase or decrease, respectively.

level (~10 nA) of the analog current measurements (Fig. 4b). More than 90% of the devices exhibit an analog on/off ratio >10^2. A high on/off ratio of the updated analog current is required in all synaptic device elements to ensure pattern recognition accuracy in an array-scale neuromorphic system[8–10]. Large currents inhibit the use of these elements in neuromorphic computing systems[12]. Thus, our Ni/PZT/LSMO memristors characterized by nanoampere readout currents are suitable for neuromorphic computing implementation.

Temporal variation of conductance, which is critical to learning accuracy, occurs at every write-read pulse operation of a synaptic device[8,48]. Figure 4c shows the final P-D curve obtained after >2.7×10^4 write-read cycles for 105 devices using an identical pulse sequence to identify temporal variation (Supplementary Fig. S18). Each curve was fit to models characterized by different temporal variations using the NeuroSim platform (Fig. 4d, see Methods)[47]. The calculated root-mean-square error (RMSE) between the experimental and simulated P-D curves was used to determine the temporal variation in each P-D response. The lowest RMSE values are obtained using the P-D curves simulated at 0.1% temporal variation for potentiation and 1.0% for depression (Fig. 4e). Thus, the potentiation and depression curves obtained after >2.7×10^4 write-read cycles in 105 devices exhibit temporal variations of <1 and <2%, respectively. In addition, the device-to-device variation for 105 Ni/PZT/LSMO devices met the requirements for high-performance neuromorphic computing (Supplementary Fig. S19). We also investigated temporal variation in Ni/PZT/LSMO memristors with thicker PZT layers (Supplementary Figs. S20 and S21). All Ni/PZT/LSMO memristors with a high on/off ratio and low temporal variation fulfill the requirements for high-performance neuromorphic computing using RRAM-based on-chip sparse learning[8,48].

Our concept focuses on set-process control using different active metal electrodes and ferroelectric electrolytes, leading to simultaneous implementation of a high analog on/off ratio and gradual synaptic weight update. Application of ECM memristors to neuromorphic computing is often difficult due to the inherently abrupt nature of the set process[48]. Lateral conduction channel growth[49,50] and appropriately designed pulse sequences with variable amplitudes and/or durations have been explored to address this issue[8]. However, lateral conduction channel growth usually produces a low analog on/off ratio[50,51], and elaborate pulse sequences increase the complexity of the peripheral circuitry and the latency and energy consumption of the device[8].

Memristors for synaptic devices require long-term memory (LTM) for long-term potentiation (LTP)[13]. Figure 5a summarizes our investigation of LTM in the Ni/PZT/LSMO memristor. A long-lived transition to a higher current level is achieved following the application of a final input pulse with an amplitude of 3.0 or 4.0 V. This condition corresponds to LTM caused by the formation of a stable conduction channel. Repeated stimulation by a 4.0-V input pulse provides extended LTM above 80000 s. However, the current obtained after application of a 2.0-V pulse rapidly returns to the HRS due to formation of an unstable conduction channel. We observe similar characteristics in Ni/PZT/LSMO memristors with thicker PZT layers (Supplementary Fig. S22).

A particularly promising mechanism regulating biological synaptic weight is STDP, through which the synaptic strengths evolve depending on the timing and causality of electrical signals from neighboring neurons[52]. We also implemented STDP using the spikes from pre- and post neurons induced by identical waveforms. When the pre- and post neuron spikes reach the artificial synapse with a delay time, △t, their superposition produces the voltage waveform, $V_{\mathrm{pre}} - V_{\mathrm{post}}$ (Fig. S23). If the resulting combined voltage waveform transitorily exceeds the minimum switching voltage, the increase/decrease in the synaptic weight corresponds to potentiation/depression depending on the sign of △t. The experimental STDP curves (Fig. 5b) reveal that only closely timed spikes produce a conductance change, whereas longer delays leave the artificial synapse unchanged. Thus, our Ni/PZT/LSMO memristor emulates the STDP behavior of a biological synapse.

Conclusions

We demonstrate that employing the same ferroelectric electrolyte in ECM memristors to control resistive switching (RS) results in neuron and synaptic devices for neuromorphic computing systems that can be selectively implemented. Thus, our Ag/PZT/LSMO memristor assembly emulates the behavior of biological neurons, including stochastic integration and firing, auto-recovery, and rapid operation. Moreover, our Ni/PZT/LSMO memristor exhibits excellent synaptic characteristics, including a high analog on/off ratio, low LRS current, good device variability, superior endurance, and long retention. The development of basic active-metal/ferroelectric systems can expedite the construction of simple, high-performance neuromorphic computing systems. To fully implement our monolithic neuron and synaptic devices in a neuromorphic computing system, the main outstanding challenge is integration of the neuron and synaptic devices on the crossbar array at the system level.

Acknowledgements

This work was supported by the National R&D Programs (No. 2022R1A2C3004135 and No. 2021M3F3A2A01037740) and Nano·Material Technology Development Program (No. 2021M3H4A1A03054864) through the National Research Foundation of Korea (NRF) funded by Ministry of Science and ICT, Korea Basic Science Institute (National research Facilities and Equipment Center) grant funded by the Ministry of Education (No. 2022R1A6C101A754), and Basic Science Research Program through the NRF funded by the Ministry of Education (No. 2022R1I1A1A01068154).

Author details

[1]Division of Quantum Phases & Devices, Department of Physics, Konkuk University, Seoul 143-701, Republic of Korea. [2]Center for Correlated Electron Systems (CCES), Institute of Basic Science (IBS), Seoul 08826, Republic of Korea. [3]Department of Physics and Astronomy, Seoul National University, Seoul 08826, Republic of Korea. [4]Graduate School of Analytical Science and Technology, Chungnam National University, Daejoen 34134, Republic of Korea

Author contributions

C.Y. and B.H.P. planned the projects and designed the experiments. C.Y. performed film growth, PFM measurements, transport measurements, conductive AFM measurements, and data analysis. G. O., S. K., J. H. J and J. H. L. assisted with the analysis of PFM data. Y.H.K. performed the TEM measurements and interpreted the results. C.Y. and B.H.P. interpreted the results, participated in discussions, and wrote the manuscript.

Conflict of interest

The authors declare no competing interests.

Publisher's note

Springer Nature remains neutral with regard to jurisdictional claims in published maps and institutional affiliations.

Supplementary information The online version contains supplementary material available at https://doi.org/10.1038/s41427-023-00481-0.

Received: 7 January 2023 Revised: 12 April 2023 Accepted: 17 April 2023.
Published online: 26 May 2023

References

1. Tuma, T., Pantazi, A., Gallo, L. M., Sebastian, A. & Eleftheriou, E. Stochastic phase-change neurons. *Nat. Nanotechnol.* **11**, 693 (2016).
2. Wang, Z. et al. Fully memristive neural networks for pattern classification with unsupervised learning. *Nat. Electron.* **11**, 137–145 (2018).
3. Zhang, X. et al. An artificial neuron based on a threshold switching memristor. *IEEE Electron Device Lett.* **39**, 308–311 (2018).
4. Wang, Z. et al. Capacitive neural network with neuro-transistors. *Nat. Commun.* **9**, 3208 (2018).
5. Zhang, X. et al. An artificial spiking afferent nerve based on Mott memristors for neurorobotics. *Nat. Commun.* **11**, 51 (2020).
6. Pickett, M. D., Medeiros-Ribeiro, G. & Williams, R. S. A scalable neuristor built with Mott memristors. *Nat. Mater.* **12**, 114–117 (2013).
7. Stoliar, P. et al. A leaky-integrate-and-fire neuron analog realized with a Mott insulator. *Adv. Func. Mater.* **27**, 1604740 (2017).
8. Chen, P.-Y. et al. Mitigating effects of non-ideal synaptic device characteristics for on-chip learning. *IEEE/ACM Int. Conf. Comput.-Aided Des.* 194–199 (2015).
9. Kim, S. et al. Pattern recognition using carbon nanotube synaptic transistors with an adjustable weight update protocol. *ACS Nano* **11**, 2814–2822 (2017).
10. Choi, S. et al. SiGe epitaxial memory for neuromorphic computing with reproducible high performance based on engineered dislocations. *Nat. Mater.* **17**, 335–340 (2018).
11. Prezioso, M. et al. Training and operation of an integrated neuromorphic network based on metal-oxide memristors. *Nature* **521**, 61 (2015).
12. Fuller, E. J. et al. Parallel programming of an ionic floating-gate memory array for scalable neuromorphic computing. *Science* **364**, 570–574 (2019).
13. Yeon, H. et al. Alloying conducting channels for reliable neuromorphic computing. *Nat. Nanotechnol.* **15**, 574–579 (2020).
14. Yoon, C. et al. Synaptic plasticity selectively activated by polarization-dependent energy-efficient ion migration in an ultrathin ferroelectric tunnel junction. *Nano Lett.* **17**, 1949–1955 (2017).
15. Wang, Z. et al. Memristors with diffusive dynamics as synaptic emulators for neuromorphic computing. *Nat. Mater.* **16**, 101–108 (2017).
16. Gao, B. et al. Ultra-low-energy three-dimensional oxide-Based electronic synapses for implementation of robust high-Accuracy neuromorphic computation systems. *ACS Nano* **8**, 6998–7004 (2014).
17. Yu, S. et al. A Low energy oxide-based electronic synaptic device for neuromorphic visual systems with tolerance to device variation. *Adv. Matter* **25**, 1774–1779 (2013).
18. van de Burgt, Y. et al. A non-volatile organic electrochemical device as a low-voltage artificial synapse for neuromorphic computing. *Nat. Mater.* **16**, 414–418 (2017).
19. Sharbati, M. T. et al. Low-power, electrochemically tunable graphene synapses for neuromorphic computing. *Adv. Mater.* **30**, 1802353 (2018).
20. Yang, C.-S. et al. All-solid-state synaptic transistor with ultralow conductance for neuromorphic computing. *Adv. Func. Mater.* **28**, 1804170 (2018).
21. Li, J. et al. Reproducible ultrathin ferroelectric domain switching for high-performance neuromorphic computing. *Adv. Mater.* **32**, 1905764 (2020).

22. Chanthbouala, A. et al. A ferroelectric memristor. *Nat. Mater.* **11**, 860–864 (2012).
23. Bao, L. et al. Dual-gated MoS_2 neuristor for neuromorphic computing. *ACS Appl. Mater. Interf.***11**, 41482–41489 (2019).
24. Izyumskaya, N. et al. Processing, structure, properties, and applications of PZT thin films. *Crit. Rev. Solid State* **32**, 111–202 (2007).
25. Chen, P.-Y., Peng, X. & Yu, S. NeuroSim+: An integrated device-to-algorithm framework for benchmarking synaptic devices and array architectures. *IEDM Tech. Dig*. 6.1.1–6.1.4 (2017).
26. Sun, W. et al. Understanding memristive switching via in situ characterization and device modeling. *Nat. Commun.* **10**, 3453 (2019).
27. Cha, J.-H. et al. Conductive-bridging random-access memories for emerging neuromorphic computing. *Nanoscale* **12**, 14339 (2020).
28. Goux, L. & Valov, I. Electrochemical processes and device improvement in conductive bridge RAM cells. *Phys. Status Solidi A.* **213**, 274–288 (2016).
29. Valov, I., Waser, R., Jameson, J. R. & Kozicki, M. N. Electrochemical metallization memories-fundamentals, applications, prospects. *Nanotechnology* **22**, 254003 (2011).
30. Valov, I. Interfacial interactions and their impact on redox-based resistive switching memories (ReRAMs). *Semicond. Sci. Technol.* **32**, 093006 (2017).
31. Lee, J. & Lu, W. D. On-demand reconfiguration of nanomaterials: when electronics meets ionics. *Adv. Mater.* **30**, 1702770 (2018).
32. Valov, I. & Lu, W. D. Nanoscale electrochemistry using dielectric thin film as solid electrolytes. *Nanoscale* **8**, 13828 (2016).
33. Yuan, F. et al. Real-time observation of the electrode-size-dependent evolution dynamic of the conducting filaments in a SiO_2 layer. *ACS Nano.* **11**, 4097–4104 (2017).
34. Liu, Q. et al. Real-time observation on dynamic growth/dissolution of conductive filaments in oxide-electrolyte-based ReRAM. *Adv. Mater.* **24**, 1844–1849 (2012).
35. Yang, Y. et al. Electrochemical dynamics of nanoscale metallic inclusions in dielectrics. *Nat. Commun.* **5**, 4232 (2014).
36. Waser, R., Dittmann, R., Staikov, G. & Szot, K. Redox-based resistive switching memories-nanoionic mechanisms, prospects, and challenges. *Adv. Mater.* **21**, 2632–2663 (2009).
37. Valov, I. & Yang, Y. Memristors with alloyed electrodes. *Nat. Nanotechnol.* **15**, 510–516 (2020).
38. Menzel, S., Böttger, U., Wimmer, M. & Salinga, M. Physics of the switching kinetics in resistive memories. *Adv. Funct. Mater.* **25**, 6306–6325 (2015).
39. Nestler, T. et al. Separators and electrolytes for rechargeable batteries: Fundamentals and perspectives. *Phys. Sci. Rev.* **4**, 20170115 (2018).
40. Li, H. et al. Fast Diffusion of multivalent ions facilitated by concerted interactions in dual-ion battery systems. *Adv. Energy Mater.* **8**, 1801475 (2018).
41. Lin, K.-L. et al. Electrode dependence of filament formation in HfO_2 resistive-switching memory. *J. Appl. Phys.* **109**, 084104 (2011).
42. Kim, S., Jung, S., Kim, M.-H., Cho, S. & Park, B.-G. Resistive switching characteristics of silicon nitride-based RRAM depending on top electrode metals. *IEICE Trans. Electron.* **E98.C**, 429 (2015).
43. Tsuruoka, T., Hasegawa, T., Terabe, K. & Aono, M. Operating mechanism and resistive switching characteristics of two-and three-terminal atomic switches using a thin metal oxide layer. *J. Electroceram.* **39**, 143–156 (2017).
44. Hughes, M. A. et al. High speed chalcogenide glass electrochemical metallization cells with various active metals. *Nanotechnology* **29**, 315202 (2018).
45. Tsuruoka, T., Terabe, K., Hasegawa, T. & Aono, M. Temperature effects on the switching kinetics of a Cu-Ta_2O_5-based atomic switch. *Nanotechnology* **22**, 254013 (2011).
46. van den Hurk, J. et al. Physical origins and suppression of Ag dissolution in GeS_x-based ECM cells. *Phys. Chem. Chem. Phys.* **16**, 18217–18225 (2014).
47. Zhang, Y. et al. Highly compact artificial memristive neuron with low energy consumption. *Small* **14**, 1802188 (2018).
48. Yu, S., et al Scaling-up resistive synaptic arrays for neuro-inspired architecture: challenges and prospect. *In 2015 IEEE International Electron Devices Meeting* 17.3 (IEEE, 2015).
49. Burr, G. W. et al. Neuromorphic computing using non-volatile memory. *Adv. Phys.* **2**, 89–124 (2017).
50. Xu, R. et al. Vertical MoS_2 double-layer memristor with electrochemical metallization as an atomic-scale synapse with switching thresholds approaching 100 mV. *Nano Lett.* **19**, 2411–2417 (2019).
51. Jang, B. C. et al. Polymer analog memristive synapse with atomic-scale conductive filament for flexible neuromorphic computing system. *Nano Lett.* **19**, 839–849 (2019).
52. Boyn, S. et al. Learning through ferroelectric domain dynamics in solid-state synapses. *Nat. Commun.* **8**, 14736 (2017).